THE SLOAN DIGITAL SKY SURVEY REVERBERATION MAPPING PROJECT: THE Hβ
RADIUS–LUMINOSITY RELATION

Gloria Fonseca Alvarez [1], Jonathan R. Trump [1], Y. Homayouni [1], C. J. Grier [2], Yue Shen [3], Keith Horne [4],
Jennifer I-Hsiu Li [3], W. N. Brandt [5][8][9], Luis C. Ho [6], B. M. Peterson [7], and D. P. Schneider [5]

ABSTRACT

Results from a few decades of reverberation mapping (RM) studies have revealed a correlation between the radius of the broad-line emitting region (BLR) and the continuum luminosity of active galactic nuclei. This "radius–luminosity" relation enables survey-scale black-hole mass estimates across cosmic time, using relatively inexpensive single-epoch spectroscopy, rather than intensive RM time monitoring. However, recent results from newer reverberation mapping campaigns challenge this widely used paradigm, reporting quasar BLR sizes that differ significantly from the previously established radius–luminosity relation. Using simulations of the radius–luminosity relation with the observational parameters of SDSS-RM, we find that this difference is not likely due to observational biases. Instead, it appears that previous RM samples were biased to a subset of quasar properties, and the broader parameter space occupied by the SDSS-RM quasar sample has a genuinely wider range of BLR sizes. We examine the correlation between the deviations from the radius–luminosity relation and several quasar parameters; the most significant correlations indicate that the deviations depend on UV/optical SED and the relative amount of ionizing radiation. Our results indicate that single-epoch black-hole mass estimates that do not account for the diversity of quasars in the radius–luminosity relation could be overestimated by an average of ∼ 0.3 dex.

Subject headings: galaxies: active – galaxies: nuclei – quasars: emission-lines – quasars: general – quasars: supermassive black holes

1. INTRODUCTION

Accurate black-hole masses are necessary to understand the growth of black holes and their role in galaxy evolution. In nearby (< 100 Mpc) galaxies, it is possible to measure black-hole mass directly from high spatial resolution observations of the dynamics of stars and gas (e.g. Kormendy & Ho 2013). But for distant active galactic nuclei[10] (AGN), the primary method to obtain reliable black-hole masses is reverberation mapping (RM) from time-domain spectroscopy (Blandford & McKee 1982; Peterson et al. 2004).

Reverberation mapping measures the time delay between variability in the continuum emission and the corresponding variability in the broad line region (BLR). In the environment around the supermassive black hole,

light from the accretion disk is absorbed and re-emitted by the BLR with a delay due to the light travel time between the two emitting regions. The time delay, multiplied by the speed of light, gives a characteristic distance to the BLR, which is assumed to be in a virial orbit around the black hole. The mass of the black hole is thus given by a virial mass calculation as in Equation (1), using the emission-line broadening (ΔV^2), characterized by the line-width FWHM or σ_{line}, combined with the radius of the BLR

$$M_{BH} = \frac{f R_{BLR} \Delta V^2}{G} \qquad (1)$$

The mass calculation includes a dimensionless factor "f", to account for the geometry of the orbit and kinematics of the BLR; this factor can be calibrated from comparing RM and dynamical masses (Onken et al. 2007; Grier et al. 2013), the $M_{\mathrm{BH}} - \sigma$ relation (Woo et al. 2015; Yu et al. 2019), or from dynamical modeling of the BLR (Pancoast et al. 2014). The f-factor is of order unity and the exact value depends on assumptions like how the broad-line velocity is measured (e.g., Peterson et al. 2004; Collin et al. 2006; Yu et al. 2019).

From RM measurements taken over the last two decades, a correlation has been observed between the measured BLR time delay and the continuum luminosity of the AGN (e.g., Kaspi et al. 2000; Bentz et al. 2009; Bentz et al. 2013). From this "radius–luminosity" ($R-L$) relation, we can estimate the radius of the BLR with just a luminosity measurement (e.g, Equation 2) and estimate the black-hole mass from single-epoch observations. This allows for the measurement of black-hole masses for a large number of AGN without high spatial resolution or long-term monitoring. However, single-epoch estimates

[1] Department of Physics, University of Connecticut, Storrs, CT 06229, USA
[2] Steward Observatory, The University of Arizona, Tucson, AZ 85721, USA
[3] Department of Astronomy, University of Illinois at Urbana Champaign, Urbana, IL 61801, USA
[4] SUPA Physics and Astronomy, University of St. Andrews, Fife, KY16 9SS, Scotland, UK
[5] Department of Astronomy & Astrophysics, The Pennsylvania State University, University Park, PA, 16802, USA
[6] Kavli Institute for Astronomy and Astrophysics, Peking University, Beijing 100871, China
[7] Department of Astronomy, The Ohio State University, Columbus, OH 43210, USA
[8] Institute for Gravitation and the Cosmos, The Pennsylvania State University, University Park, PA, 16802, USA
[9] Department of Physics, The Pennsylvania State University, University Park, PA, 16802, USA

[10] Throughout this work, we generically use the terms "quasar" and "AGN" interchangeably to refer to broad-line AGN, as broad lines are necessary for reverberation mapping.

are only correct if the $R-L$ relation accurately describes the diverse AGN population; therefore, it is necessary to measure this relation over a broad AGN sample and with the least bias possible.

Bentz et al. (2013) used Hβ time-lag measurements and reliable subtraction of host galaxy light for 41 AGN from different RM campaigns to determine the following $R-L$ relation between the mean radius of the Hβ-emitting BLR and the AGN continuum luminosity at 5100 Å (λL_{5100}) :

$$\log(R_{\rm BLR}/\text{lt-day}) = K + \alpha \log(\lambda L_{5100}/10^{44} \text{ erg s}^{-1}) \quad (2)$$

The slope of this relation ($\alpha = 0.533$) is consistent with the $R_{\rm BLR} \propto L^{0.5}$ expectation from basic photoionization models (Davidson 1972). Bentz et al. (2013) measured an intrinsic scatter in the relation of $\sigma \sim 0.19$, and a normalization $K = 1.527$. The Bentz et al. (2013) $R-L$ relation has been the recent standard used to estimate single-epoch black hole masses; however, recent RM results appear to deviate from this relation.

The Sloan Digital Sky Survey Reverberation Mapping (SDSS-RM) project is a dedicated multi-object RM campaign that has been monitoring 849 quasars with spectroscopy and photometry since 2014 (Shen et al. 2015b). Grier et al. (2017) published an Hβ $R-L$ relation for 44 AGN from the first year of SDSS-RM monitoring. The time lags measured by SDSS-RM are often significantly shorter than those predicted by Equation (2) for their given AGN luminosity, and thus these sources fall below the Bentz et al. (2013) $R-L$ relation. In addition, the Super-Eddington Accreting Massive Black Holes (SEAMBH) survey presented a $R-L$ relation for a sample of rapidly-accreting AGN that also differs from Bentz et al. (2013) in the same manner (Du et al. 2016, 2018; Du & Wang 2019).

In this work we examine if this discrepancy is due to observational biases that restrict the allowable lag detections, or if the SDSS-RM and SEAMBH samples have properties that represent a broader population of AGN compared to previous RM studies; thus indicating a physical origin for the discrepancy, as suggested by recent work (Czerny et al. 2019; Du & Wang 2019). We explore this by simulating a $R-L$ relation based on Bentz et al. (2013), while imposing the observational constraints of the SDSS-RM dataset. We present the data included in our study in Section 2, and provide a detailed description of our simulated $R-L$ relation and results in Section 3. In Section 4, we discuss possible causes for the discrepancy. Throughout this work we assume a standard ΛCDM cosmology with $\Omega_\Lambda = 0.7$, $\Omega_M = 0.3$, and $H_0 = 70$ km s^{-1} Mpc^{-1}.

2. DATA

For our analysis, we compare Hβ lags, λL_{5100}, and the best-fit $R_{\rm BLR}-\lambda L_{5100}$ relation for the Bentz et al. (2013), Grier et al. (2017), and Du et al. (2016, 2018) datasets. The lags for the 3 RM campaigns were measured using different methods: Bentz et al. (2013) and Du et al. (2016, 2018) used the interpolated cross-correlation function (ICCF, Gaskell & Peterson 1987; White & Peterson 1994; Peterson et al. 2004), while Grier et al. (2017) primarily used JAVELIN (Zu et al. 2011) and CREAM (Starkey et al. 2016). JAVELIN and CREAM use different assumptions than ICCF but are designed to produce
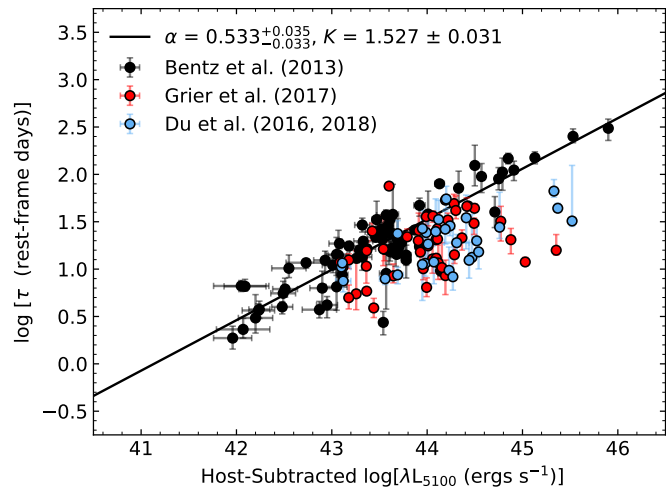

FIG. 1.— The $R-L$ relation for Hβ time lags from Bentz et al. (2013), Grier et al. (2017), and Du et al. (2016, 2018). The black line shows the $R-L$ relation from Bentz et al. (2013), with a slope $\alpha = 0.533$ and a normalization $K = 1.527$. The lag measurements from SDSS-RM (Grier et al. 2017) and SEAMBH (Du et al. 2018) frequently lie below the $R-L$ relation established by Bentz et al. (2013).

similar results, so any deviations from the Bentz et al. (2013) $R-L$ relation should not be due to the different lag detection methods, as discussed in section 2.3. We briefly describe the details of the lag measurement methods in section 2.1.

Figure 1 presents the $R-L$ relation for the Bentz et al. (2013), Grier et al. (2017), and Du et al. (2016, 2018) samples of AGN with Hβ RM lags. We describe these three samples in detail in the subsections below. The distribution of AGN properties in each sample is presented in Figure 2. For the Eddington ratio ($\lambda_{\rm Edd} = \frac{L_{\rm bol}}{L_{\rm Edd}}$), we assume $L_{\rm bol} = 5.15\lambda L_{3000}$ and $L_{\rm bol} = 9.26\lambda L_{5100}$ (Richards et al. 2006). Published 3000 Å luminosities are available only for 41 of the Grier et al. (2017) AGN; we use the 5100 Å luminosities for all other AGN in the three samples. We use black-hole masses for the Bentz et al. (2013) sample from the compilation of Bentz & Katz (2015). In all three samples, the AGN luminosities are host-subtracted, and as such the luminosity uncertainties include a contribution from the uncertainty associated with the host-galaxy decomposition. In general this means that the AGN luminosity uncertainties are largest for low-luminosity and host-dominated AGN, and are generally small for luminous AGN. We determine the best-fit $R-L$ relation for each sample employing multiple linear regression with the python MCMC software PyMC3, including uncertainties in both radius (y-axis) and luminosity (x-axis) and allowing for excess intrinsic scatter.

2.1. Lag Measurement Methods

The ICCF determines the cross-correlation between two light curves, measured as the Pearson correlation coefficient r as a function of time delay τ. Because the data are unevenly spaced due to observational constraints, the ICCF linearly interpolates the first light curve to produce overlapping points to calculate r for any delay τ. The same process is repeated starting with the second light curve shifted by $-\tau$. The cross-correlation coefficient for a given τ is obtained by averaging the two values of r.
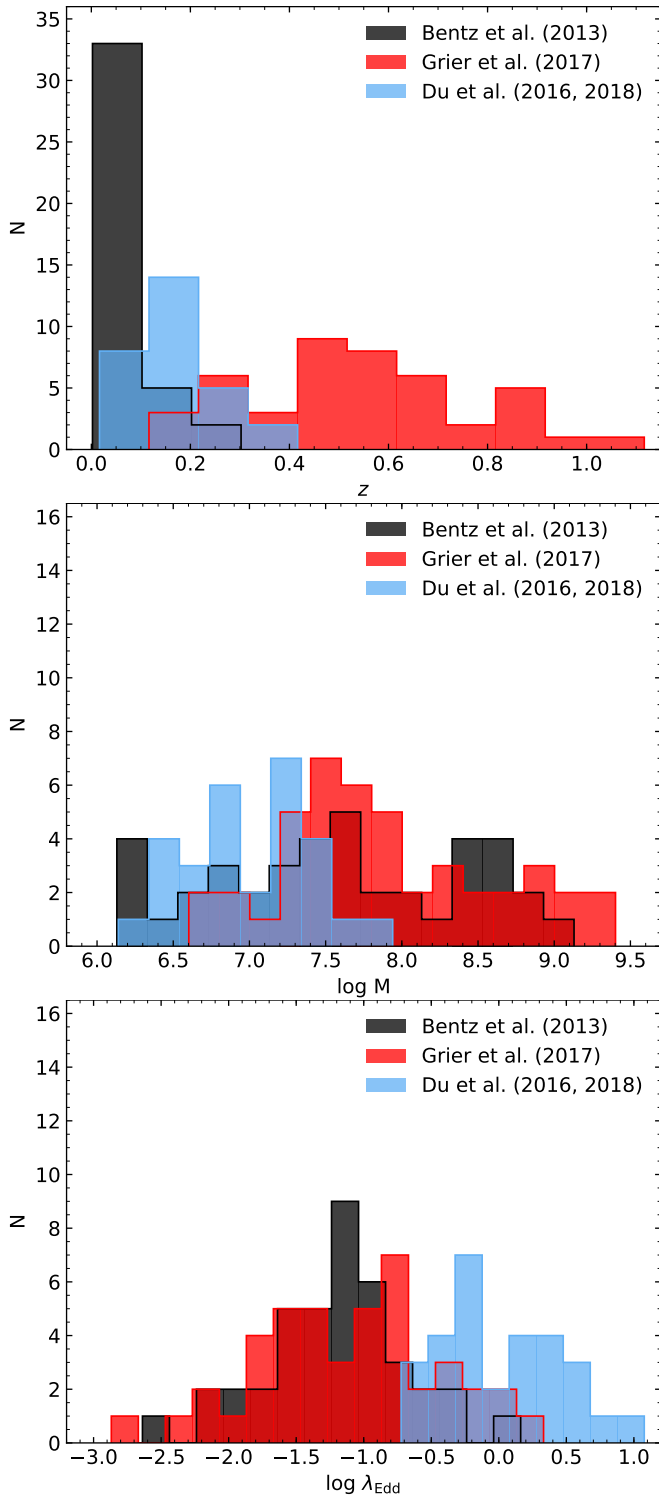
Fig. 2.— From top to bottom: Distribution of redshift, mass, and λ_{Edd} for the Bentz et al. (2013), Grier et al. (2017) and Du et al. (2016, 2018) samples.

The ICCF repeats this procedure for a range of τ, to obtain the final cross-correlation function (CCF). The likely time lag between the two light curves is given by the centroid of the CCF. The uncertainties are calculated using Monte Carlo methods with flux re-sampling and random subset sampling (Peterson et al. 2004).

Instead of using linear interpolation, JAVELIN as-

sumes that the variability of the continuum light curve is best described by a damped random walk (DRW) model. JAVELIN then models the BLR light-curve response with the same DRW model combined with a top-hat transfer function centered at a lag τ, producing a BLR light curve model that is a shifted, smoothed, scaled version of the continuum light curve. Markov Chain Monte Carlo (MCMC) is used to identify the most likely lag and uncertainty. CREAM adopts a similar approach to JAVELIN to measure lags, with the same DRW assumption about variability, but with a slightly different treatment of the uncertainties. Detailed simulations by Li et al. (2019) and Yu et al. (2020) find that, for lightcurves of similar cadence and noise to SDSS-RM, JAVELIN produces more accurate lags and lag uncertainties than ICCF, and fewer false positives. Grier et al. (2017) measured Hβ lags using JAVELIN, ICCF, and CREAM; in this work we primarily utilize the lags from JAVELIN and CREAM, while noting that the ICCF lags of SDSS-RM quasars produce the same offset in the $R-L$ relation (Figure 5).

2.2. Bentz et al.

Bentz et al. (2013) collected a sample of 41 AGN from previous RM surveys, focusing on adding accurate host-galaxy subtraction from HST imaging. The sample primarily includes nearby AGN that were generally selected to be apparently bright and variable, with luminosities in the range $10^{42} < \lambda L_{5100,\mathrm{AGN}} < 10^{46}$ ergs s^{-1}. The AGN have lags measured from observing campaigns with monitoring durations that ranged from 64 to 120 days, with cadences as rapid as 1 day between observations. Lags were measured using the ICCF method, resulting in 70 Hβ time lags for 41 unique AGN in the range 2–100 rest-frame days.

The luminosity measurements are corrected for host-galaxy contributions; this is especially important for lower-luminosity AGN since galaxy contamination leads to an overestimation of λL_{5100}, steepening the $R-L$ relation. Previous RM surveys that did not correct for host-galaxy luminosity found a steeper $R-L$ relation with a slope $\alpha \sim 0.70$ (Kaspi et al. 2000). Bentz et al. (2013) measured the host-galaxy contribution for each AGN through morphological decomposition of HST/ACS images, using the GALFIT software (Peng et al. 2002) to determine the best-fit point-source AGN and extended galaxy surface brightness profiles implementing a nonlinear least-squares fit algorithm.

Figure 11 in Bentz et al. (2013) presents the $R-L$ relation observed for their measured Hβ time lags, with a slope $\alpha = 0.533^{+0.035}_{-0.033}$ and a normalization $K = 1.527^{+0.031}_{-0.031}$ for the best-fit line. Our fitting method yields a nearly identical slope $\alpha = 0.52 \pm 0.03$ and a normalization $K = 1.52 \pm 0.03$ for the Bentz et al. (2013) Hβ lags.

2.3. SDSS-RM

Grier et al. (2017) successfully measured Hβ time lags for 44 AGN from the SDSS-RM survey. The AGN have luminosities $10^{43} < \lambda L_{5100,\mathrm{AGN}} < 10^{45.5}$ ergs s^{-1} and redshifts $0.12 < z < 1$. The full SDSS-RM sample is magnitude-limited (by $i_{\mathrm{AB}} < 21.7$), with no other selection criteria for AGN properties. This results in a sample
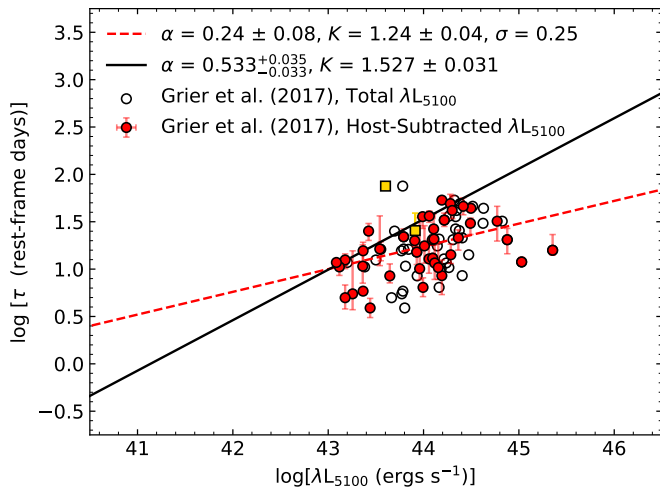
FIG. 3.— The $R-L$ relation for 44 AGN in the SDSS-RM survey, with Hβ time lags from Grier et al. (2017) and λL_{5100} from Shen et al. (2015a). Out of the 44 lags, 32 were measured using JAVELIN and 12 were measured using CREAM. The open circles have λL_{5100} that includes host-galaxy light, while the solid red circles have AGN luminosities (λL_{5100}) that are host-subtracted using principal component analysis of the coadded spectra. Our best-fit line for the red (host-subtracted) points is shown as the red dashed line, with a slope $\alpha = 0.24 \pm 0.08$ and a normalization of $K = 1.24 \pm 0.04$ that both differ from the Bentz et al. (2013) best-fit $R-L$ relation (shown as the black solid line) by $> 3\sigma$. The two square points were excluded from the fitting (see text for details). The SDSS-RM AGN generally have lags that are shorter than expected from the Bentz et al. (2013) $R-L$ relation at a given host-subtracted λL_{5100}.

FIG. 4.— The $R-L$(Hβ) relation for the 44 SDSS-RM AGN, with Hβ time lags from Grier et al. (2017) and broad-line Hβ luminosity from Shen et al. (2019). Black solid and dashed lines show the relation between Hβ time lags and $L_{H\beta}$ from Kaspi et al. (2005) for two different fitting methods. The SDSS-RM AGN have lags that fall below the $R-L$(Hβ) relation.

that is more representative of the general AGN population, and a greater diversity in redshift and other AGN properties compared to previous RM studies. For example, the SDSS-RM sample spans a much broader range of emission-line widths, strengths, and blueshifts compared to the sample of Bentz et al. (2013) (see Figure 1 of Shen et al. 2015b).

Spectra of the quasars were obtained using the Baryon Oscillation Spectroscopic Survey (BOSS) spectrograph (Smee et al. 2013) on the SDSS 2.5 m telescope (Gunn et al. 2006) at Apache Point Observatory. The initial observations include 32-epochs taken over a period of 6 months in 2014. The exposure time for each observation was ~ 2 hr and the average time between observations was 4 days (maximum 16.6 days).

Photometric observations were acquired in the g and i filters with the Bok 2.3 m telescope and the Canada-France-Hawaii Telescope (CFHT). Additionally, synthetic photometric light curves were produced from the BOSS spectra in the g and i bands. All of the g and i band light curves were merged using the CREAM software (Starkey et al. 2016) to create a continuum light curve for each AGN (see Grier et al. 2017, for additional details of the light-curve merging procedure).

Grier et al. (2017) measured Hβ reverberation lags using ICCF, JAVELIN and CREAM. Each method used a lag search range between -100 and 100 days, given the length of the SDSS-RM observation baseline (~ 200 days). This resulted in 32 lags from JAVELIN and 12 from CREAM, only including "reliable" positive time lags that have SNR > 2, a single well-defined peak in the lag probability distribution function, and a correlation coefficient of $r_{\max} > 0.45$.
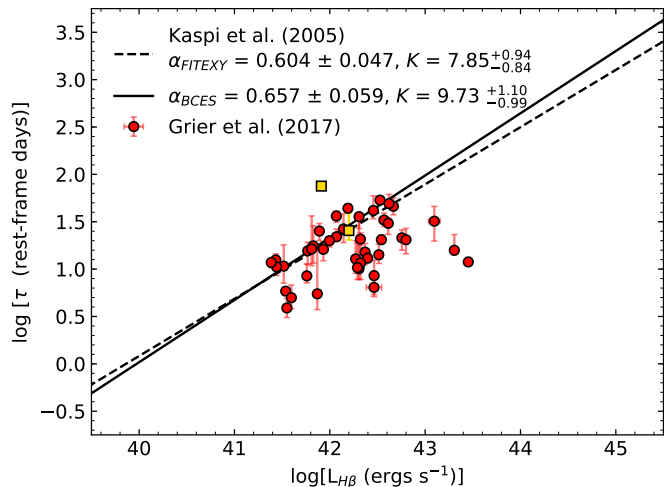
Shen et al. (2015b) used principal component analysis

(PCA) to decompose the quasar and host-galaxy spectra, assuming that the total spectrum is a combination of linearly independent sets of quasar-only and galaxy-only eigenspectra. The SDSS eigenspectra are taken from Yip et al. (2004). To obtain the quasar-only spectrum, Shen et al. (2015b) subtracted the best-fit host-galaxy spectrum from the total spectrum. Yue et al. (2018) independently estimated the host-galaxy contribution using imaging decomposition and found consistent results to the spectral decomposition.

Figure 3 presents the relation between the 44 SDSS-RM Hβ time lags and λL_{5100}. Host-subtracted continuum luminosity (λL_{5100}) measurements were taken from Shen et al. (2015a). The points in red represent AGN luminosities that are host-subtracted as described above. The observed rest-frame time lags are generally shorter than predicted from the Bentz et al. (2013) $R-L$ relation. The SDSS-RM data exhibit a positive correlation between radius and luminosity, with a Spearman's $\rho = 0.54$ and a null probability of no correlation of $p \sim 0.0$. The $R-L$ properties of the SDSS-RM quasars are best fit by a line with shallower slope and lower normalization, as shown as the red best-fit line of slope $\alpha = 0.24 \pm 0.08$ and a normalization $K = 1.24 \pm 0.04$. However, the limited dynamic range of the SDSS-RM quasars means that the data could also be consistent with the same $\alpha \simeq 0.5$ slope of the Bentz et al. (2013) data, with an average offset of shorter lags in SDSS-RM quasars over a range of continuum luminosities. Fitting the same SDSS-RM data, while fixing the slope to be 0.533, results in the same lower normalization K $= 1.24 \pm 0.05$. For this and all subsequent least-squares fitting, we exclude the SDSS-RM data point with the longest lag and smallest fractional uncertainty as an outlier (RMID 781). We also exclude the hyper-variable quasar RMID 017, as it increases in luminosity by a factor of ~ 10 over the span of the SDSS-RM monitoring (Dexter et al. 2019).

Figure 3 also includes the total λL_{5100} without host-galaxy subtraction for each AGN as open circles, as an indication of the typical relative contribution of AGN and galaxy light. We further demonstrate that the $R-L$
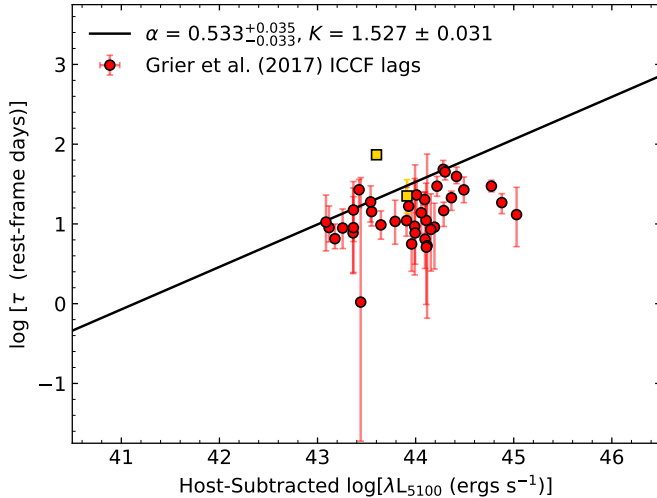
FIG. 5.— The $R - L$ relation for 39 ICCF lags of the SDSS-RM AGN from Grier et al. (2017) with host-subtracted λL_{5100} from Shen et al. (2015a). Five AGN have ICCF lags less than 1 day and are not shown in the figure. The ICCF lags of SDSS-RM AGN have the same offset from the Bentz et al. (2013) $R - L$ relation seen in Figure 3.

offset is not due to under-subtracted host-galaxy luminosities by examining the $R - L(\text{H}\beta)$ relation, presented in Figure 4. The luminosity from the Hβ emission line is produced by the AGN broad-line region and does not have any galaxy contribution. Since the Bentz et al. (2013) sample lacks published Hβ luminosities, we cannot compare that sample with the SDSS-RM $R - L(\text{H}\beta)$ relation. Instead, we use the Kaspi et al. (2005) best-fit $R - L(\text{H}\beta)$ lines that were fit to a subset of the Bentz et al. (2013) data, shown as dashed and solid lines in Figure 4. The SDSS-RM lags show the same general trend of falling below the relation measured from previous RM data.

Finally, to be certain that the different lag-detection methods are not the cause of the offset, we present the $R - L$ relation using ICCF measured lags from SDSS-RM in Figure 5. The ICCF lags fall below the Bentz et al. (2013) relation just as seen in the JAVELIN and CREAM lags.

2.4. SEAMBH

The SEAMBH project is a RM campaign spanning 5 years of monitoring (Du et al. 2016, 2018). The AGN in the sample were selected from SDSS using a dimensionless accretion rate $\dot{\mathcal{M}}$, derived from the standard thin-disk equations (Wang et al. 2014b):

$$\dot{\mathcal{M}} = 20.1 \left(\frac{L_{44}}{\cos i} \right)^{3/2} m_7^{-2} \quad (3)$$

The inclination of the disk is given by i and we assume $\cos i = 0.75$ (Du et al. 2018). The luminosity and mass dependence are parameterized as $L_{44} = \lambda L_{5100}/10^{44}$ and $m_7 = M/10^7 \, M_\odot$, respectively. The SEAMBH AGN were selected to have $\dot{\mathcal{M}} > 3$; the sample of 29 AGN has $10 < \dot{\mathcal{M}} < 10^3$, giving them higher accretion rates than the general AGN population. For comparison, the Bentz et al. (2013) and Grier et al. (2017) samples have a median $\dot{\mathcal{M}} < 0.50$. Spectroscopic and photometric observations were made over 5 years with the Lijiang 2.4 m
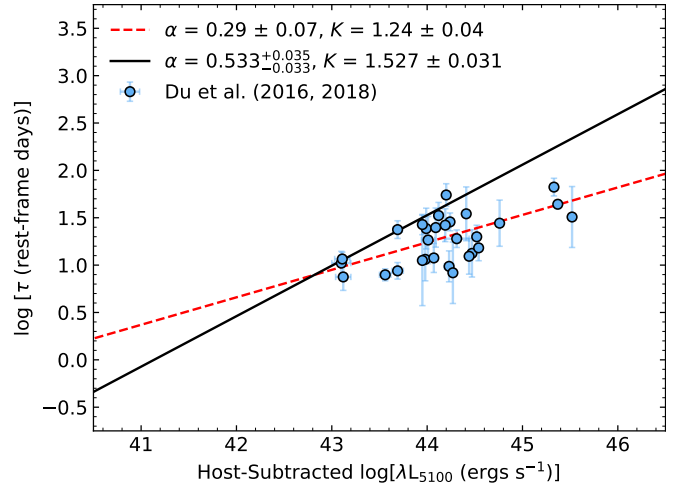

FIG. 6.— The $R - L$ relation for the 29 Hβ time lags measured by Du et al. (2016, 2018). The time lags were measured using ICCF and include 19 lags from Du et al. (2016) and 10 lags from Du et al. (2018). The AGN luminosities (λL_{5100}) were calculated using a galaxy-contribution estimate based on Equation (4). Our best-fit line, shown as a dashed red line, gives a slope $\alpha = 0.29 \pm 0.07$ and a normalization $K = 1.24 \pm 0.04$, indicating that the SEAMBH AGN (like the SDSS-RM AGN) follow a relation that is significantly below the previous Bentz et al. (2013) $R - L$ relation.

telescope, averaging 90 nights per object. Typical exposure times were 10 minutes for photometry and 1 h for spectroscopy. Du et al. (2016, 2018) used an empirical relation to determine the host-galaxy contribution to the spectrum based on λL_{5100}, derived by Shen et al. (2011) for SDSS fiber spectra:

$$\frac{L_{5100}^{\text{host}}}{L_{5100}^{\text{AGN}}} = 0.8052 - 1.5502x + 0.912x^2 - 0.1577x^3 \quad (4)$$

Here $x = L_{5100}^{\text{tot}} \times 10^{-44}$ ergs s^{-1}. For spectra with $L_{5100}^{\text{tot}} > 1.053 \times 10^{44}$ ergs s^{-1}, the host-galaxy contribution was assumed to be zero.

The $R - L$ relation for the 29 SEAMBH Hβ lags measured by Du et al. (2016, 2018) is presented in Figure 6. Similar to the SDSS-RM data in Figure 3, the measured lags are shorter than expected from Equation (2), resulting $R - L$ relation with a shallower slope $\alpha = 0.29 \pm 0.07$ and a lower normalization $K = 1.24 \pm 0.04$. The SEAMBH data, like the SDSS-RM data, cover a limited dynamic range on both axes, and also appear consistent with a slope of $\alpha \simeq 0.5$ with an average offset for shorter lags over a broad range of continuum luminosity.

3. SIMULATING OBSERVATIONAL BIAS ON THE $R - L$ RELATION

The effects of the SDSS-RM observational limits on the observed $R - L$ relation are not easily predictable. For instance, the sample is magnitude-limited in the i band, rather than limited by the luminosity used for the R-L relation. There are also constraints on the length of the measurable lags due to the duration and cadence of the observations. In order to examine how observational biases affect the $R - L$ relation, we simulated a $R - L$ relation starting from Bentz et al. (2013) (Equation 2) and including observational errors and limits appropriate for the SDSS-RM monitoring campaign.
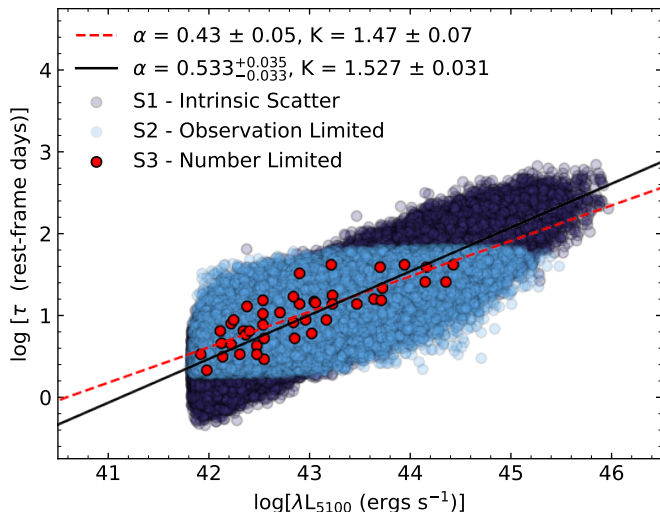
3.1. General Simulation

FIG. 7.— One iteration of the simulated Hβ $R - L$ relation. Points in purple represent the relation for AGN in sample S1, which includes only the intrinsic scatter in Bentz et al. (2013). Points in blue represent the AGN in sample S2, which takes into account observational errors and observational limits typical of SDSS-RM. The points in red are 44 random points chosen from sample S2, this accounts for the number of lags detected by SDSS-RM. The red line shows the best fit for the points in red (S3).

To create a representative sample of AGN, we generated 10^7 random AGN luminosities in the range 10^{42}–10^{46} ergs s^{-1} following the i-band luminosity function from Ross et al. (2013):

$$\Phi = \frac{\Phi^*}{(L/L_B^*)^{3.37} + (L/L_B^*)^{1.16}} \quad (5)$$

The $L^{3.37}$ and $L^{1.16}$ terms represent the bright and faint end of the distribution, respectively, with a break luminosity $L_B^* = 10^{44.62}$ ergs s^{-1}. This results in a distribution of AGN luminosities in the observed i-band. To shift the observed i-band luminosities to λL_{5100} we use the average quasar SED of Richards et al. (2006) and a randomly assigned redshift. Each simulated AGN was assigned a redshift randomly drawn from the set of 44 SDSS-RM AGN and spanning $0.2 < z < 1.2$.

We calculated the expected radius of the Hβ BLR (given as $\tau = R/c$ in days) for each λL_{5100} using the Bentz et al. (2013) relation, including an intrinsic scatter of $\sigma_{\rm int} = 0.19$. The BLR radius for each of the 10^7 simulated AGN was initially calculated following the relation $\log \tau = K + \alpha(\log L - 44) + R(\sigma_{\rm int})$, where $R(\sigma_{\rm int})$ is a random number drawn from a normal distribution with a standard deviation of $\sigma_{\rm int}$. For a given luminosity, this process produced τ above or below the Bentz et al. (2013) line. We designate this sample S1, shown in Figure 7 as purple data points. Figure 7 presents one iteration of the complete simulation.

3.2. Observational Limits

The SDSS-RM observational selection effects were applied to the simulations by adding observational uncertainties as well as lag and magnitude limits to the S1 sample. First, observational uncertainties were assigned to each of the simulated AGN by randomly drawing luminosity and lag uncertainties (σ_L and σ_τ) from the actual 44 SDSS-RM λL_{5100} and τ measurements

(Shen et al. 2015a; Grier et al. 2017). We then replicated the sample limits of SDSS-RM by imposing the same lag and magnitude constraints as the observations. Simulated AGN were restricted to observed-frame lags $4 < \tau_{\rm obs} < 75$ days, and i-band magnitude < 21.7.

The average cadence for SDSS-RM observations was 4 days, which places a lower limit on the possible observed-frame time lags. Conversely the upper limit of 75 days comes from the longest measured time lag from SDSS-RM, related to the monitoring duration of 180 days and the need for overlap between the continuum and emission-line light curves.

While the observed-frame lag limit can be implemented by a simple redshift conversion, several additional steps were required to fully emulate the magnitude limits of the observed SDSS-RM sample. The SDSS-RM parent sample of quasars is restricted to total (AGN+host) magnitudes of $i < 21.7$, but the S1 sample has AGN-only luminosities at rest-frame 5100 Å. We add a host-galaxy contribution to the simulated AGN luminosities following Equation (4) (measured for similar SDSS AGN spectra by Shen et al. 2011). We assume a 0.35 dex scatter in this relation, since 0.35 dex is the standard deviation of the actual host-galaxy luminosities of the SDSS-RM quasars. We convert this total λL_{5100} to i-band magnitude before implementing a magnitude cutoff. However, there is an additional magnitude dependence of the lag detection that must be considered, as lags are easier to recover for brighter AGN: the fraction of AGN from SDSS-RM with detected lags by Grier et al. (2017) is roughly 1/3 as high for $i > 20$ AGN as for $i < 20$ AGN. We account for this by removing all AGN with $i > 21.7$ and keeping all AGN with $i < 20$, and only keeping 1/3 of AGN with $20 < i < 21.7$.

We designate this "observation-limited" sample S2, shown as blue points in Figure 7. The boundaries in rest-frame lag and luminosity are smooth rather than sharp due to the range of redshifts applied to the simulated sample, and are slightly tilted because both the observed-frame lag and magnitude limits depend on redshift to convert to the rest-frame lag and luminosity.

Finally, to account for the limit in the number of actual lag detections in SDSS-RM (44 measured lags), we randomly selected 44 points from S2; we designate this "number-limited" sample S3. The S3 sample for one of the simulations is shown as the red points in Figure 7.

3.3. Fitting the Simulated $R - L$ relation

We repeated the random selection of 44 points and best-fit line 2000 times to see how observing specific AGN affected the slope of the simulated relation. We used the python package PyMC3 to determine the best-fit $R - L$ relation for each of the 2000 simulations, with one example of this fit shown by the dashed red line in Figure 7. The distribution of best-fit line parameters from the 2000 simulations is presented in Figure 8. The simulated best-fit $R - L$ relations have a median slope $0.43^{+0.04}_{-0.04}$, and a median normalization of $1.42^{+0.04}_{-0.05}$; here the plus and minus values represent the 16% and 84% percentiles of the distribution of slopes and normalizations, not the uncertainty in the fit. The slope and normalization are consistent (2.6σ and 2.7σ, respectively) with the Bentz et al. (2013) $R - L$ relation (represented by the black

point in Figure 8). Only $< 1\%$ of the simulations have best-fit slopes and normalizations that are as extreme as the best-fit $R - L$ relation for the observed SDSS-RM data. This result suggests that observational biases are unlikely to be the main cause of the different $R - L$ relation represented by SDSS-RM AGN compared to previous RM samples.

To examine if the number of detected lags by SDSS-RM affects the $R - L$ relation, we can increase the number of selected points to reflect the future number of detected Hβlags. The Black Hole Mapper in the upcoming SDSS-V will allow RM of over 1000 quasars (Kollmeier et al. 2017). We estimate that this will increase the number of Hβ lags to ~ 100. Here we assume the SDSS-RM observational effects applied to the simulations are also a reasonable approximation for the SDSS-V observations. The distribution of best-fit lines for the 100 random points has a median slope $0.43^{+0.03}_{-0.03}$ and normalization of $1.42^{+0.03}_{-0.03}$. Here the best-fit slope and normalization that are inconsistent (by 3.5σ) with the Bentz et al. (2013) best-fit line, suggesting that a larger sample will better constrain the effects of observational bias. The narrower distribution of best-fit lines is even less likely than the smaller simulated sample to match the observed SDSS-RM $R - L$ relation, with less than 1% of the simulated best-fit $R - L$ relations as extreme as the best fit to the SDSS-RM observations.

Since slope and normalization are degenerate parameters in the best-fit $R - L$ relation, and considering the limited range in SDSS-RM luminosities, we additionally repeated the fitting procedure with slope fixed to the Bentz et al. (2013) value of $\alpha = 0.533$ and only allowed the normalization K to vary. This effectively tests if the simulations of observational bias can reproduce the $R-L$ offset of the SDSS-RM AGN. The mean normalization for the distribution is $K = 1.53^{+0.03}_{-0.03}$, again consistent with $K = 1.527$ from Bentz et al. (2013) and $> 5\sigma$ inconsistent with the observed $R - L$ offset of the SDSS-RM data.

In general the simulations of observational bias produce a $R - L$ relation that is statistically consistent with the Bentz et al. (2013) best-fit relation, with only marginally flatter slopes and lower normalizations. Less than 1% of the simulations produce best-fit $R - L$ relations that are as extreme as the observed SDSS-RM and SEAMBH $R - L$ data. Li et al. (2019) arrived at a similar conclusion using independent light-curve simulations, additionally noting that JAVELIN lags measured from SDSS-RM data are unlikely to include enough false positive detections to strongly influence the measured $R - L$ relation.

Our simulations suggest that observational bias is unlikely to be the main cause of the SDSS-RM and SEAMBH AGN lags falling below the Bentz et al. (2013) $R-L$ relation. In the next section we investigate the possibility that $R-L$ offsets are instead driven by physical AGN properties.

4. PROPERTIES OF QUASARS OFFSET FROM THE $R - L$ RELATION

The $R - L$ differences between SDSS-RM and Bentz et al. (2013) may exist because the SDSS-RM sample spans a broader range of quasar properties (Shen et al. 2015a, 2019). The SEAMBH sample also occupies a very different parameter space compared to the Bentz et al.
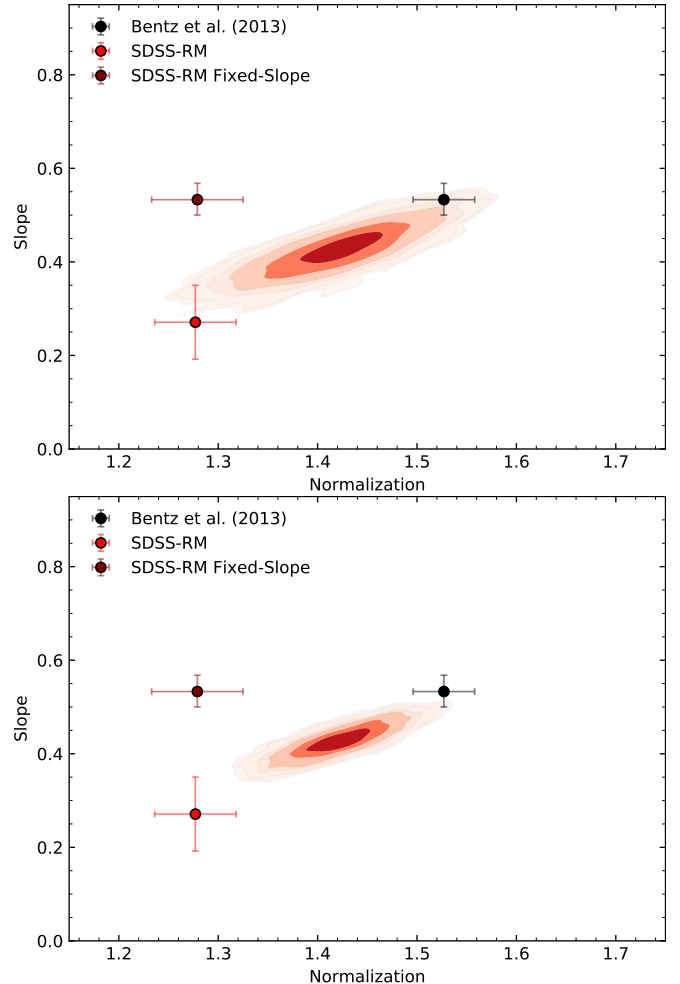

FIG. 8.— *Top:* The distribution of slopes and normalizations from fitting 44 random points from our simulated sample, shown as red contours that include 38% (0.5σ), 68% (1σ), 86% (1.5σ), 95% (2σ), 98% (2.5σ) and 99% (3σ) of the distribution. The red point represents the fitting results for SDSS-RM (Figure 3). The black point represents the result from Bentz et al. (2013). The dark red point represents the fitting result for SDSS-RM keeping the slope fixed to be the same as Bentz et al. (2013). The SDSS-RM measurement falls outside the 3σ contour and is only $< 1\%$ likely to be produced by the simulation of observational bias. The Bentz et al. (2013) measurement falls just outside the 2σ contour and is consistent with 5% of the simulated $R-L$ parameters. *Bottom:* The distribution of slopes and normalization for 100 random points from the simulated sample, using the same enclosed probabilities for the contour levels. The SDSS-RM point is outside the 3σ contour and so is again only $< 1\%$ likely to be consistent with the simulation. In both cases, observational bias is insufficient to explain the $R - L$ offsets of the SDSS-RM quasars.

(2013) sample, as SEAMBH AGN were specifically selected to have higher Eddington ratios.

In this section, we investigate how the offset from the Bentz et al. (2013) $R - L$ relation depends on various AGN properties. We define this offset as the ratio between the measured rest-frame Hβ lag $\tau_{\rm obs}$ and the expected time lag τ_{R-L} from Equation (2) for the given AGN λL_{5100}. We calculate the offset $(\tau_{\rm obs}/\tau_{R-L})$ for each of the AGN in Grier et al. (2017), Bentz et al. (2013), and Du et al. (2016, 2018). In the subsequent analyses, we report the significance of each correlation in terms of the factor of sigma by which its slope is inconsistent from zero, using 3σ as our threshold for a significant
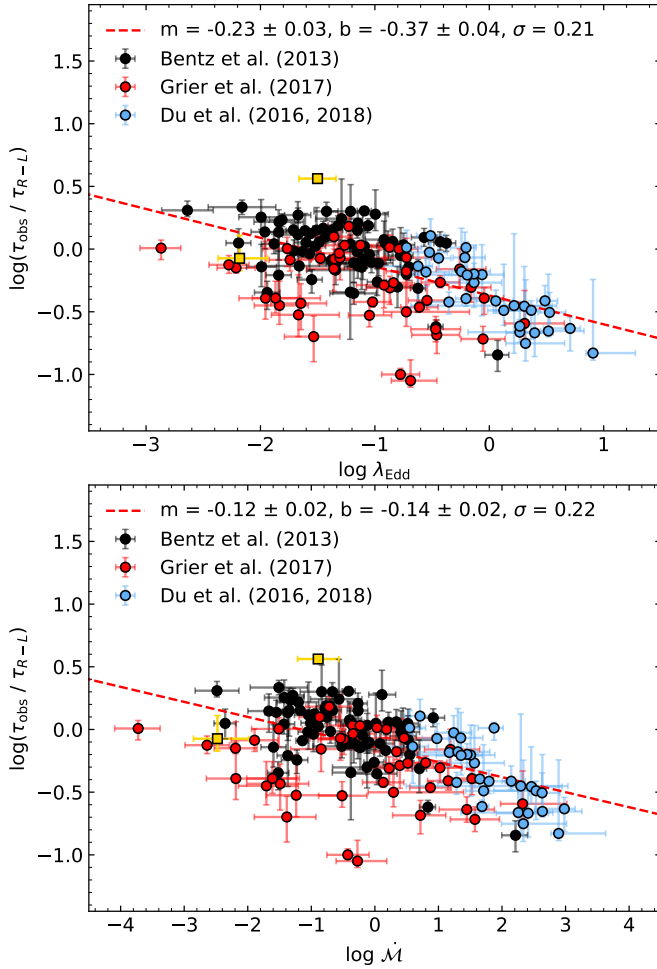
FIG. 9.— The $R - L$ offset $\tau_{\rm obs}/\tau_{R-L}$ of the three RM samples with Eddington ratio $\lambda_{\rm Edd}$ (top) and the pseudo accretion rate $\dot{\mathcal{M}}$ (see Equation 3). In both cases there is a significant anti-correlation between the two quantities, with the best-fit lines shown in red. The best-fit lines have slopes m that are $> 5\sigma$ different from zero, and a Spearman's $\rho \sim -0.50$ with a null-probability value of $p \sim 10^{-11}$. However, these trends are difficult to interpret since the two axes are self-correlated. We find much weaker correlations when comparing $R-L$ offsets to uncorrelated quantities associated with accretion rate, as seen in Figures 10 and 11.

correlation.

4.1. $R - L$ Offset with Accretion Rate

Du et al. (2016, 2018) propose that the $R - L$ offsets are driven by accretion rate, with more rapidly accreting AGN having shorter lags at fixed λL_{5100}. They suggest that radiation pressure in rapidly accreting AGN causes the inner disk to be thicker (a "slim" disk), causing self-shadowing of the disk emission that reduces the ionizing radiation received by the BLR and thus decreases its radius (Wang et al. 2014a). The self-shadowing does not affect the optical continuum emission used in the $R - L$ relation, so the broad-line lags are shorter than expected for a given observed λL_{5100}. However, a correlation between offset and accretion rate is expected not just from quasar properties but simply because the axes are correlated: the y-axis ($\tau_{\rm obs}/\tau_{R-L}$) is a log-ratio of $\tau/\lambda L_{5100}{}^{0.5}$, while the x-axes ($\lambda_{\rm Edd}$, $\dot{\mathcal{M}}$) include log-ratios of $\lambda L_{5100}/\tau$ and $\lambda L_{5100}{}^{1.5}/\tau^2$, respectively.

Despite these self-correlations, for direct comparisons
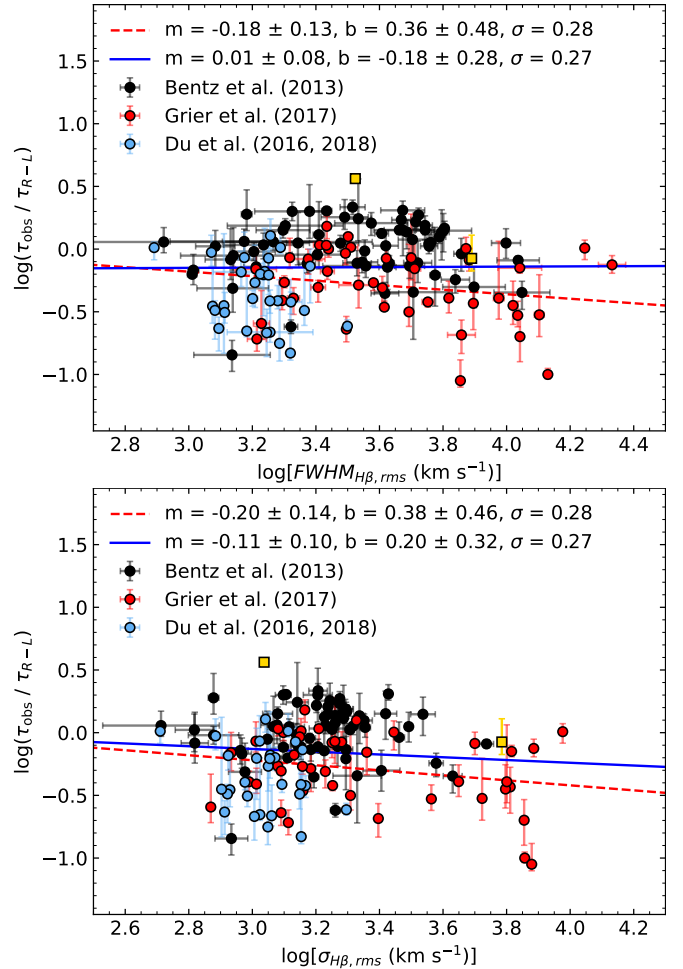
FIG. 10.— The $R - L$ offset of AGN in all three samples with FWHM$_{\rm H\beta}$ (top panel) and $\sigma_{\rm H\beta}$ (bottom panel). For the Bentz et al. (2013) sample, the linewidths were taken from Bentz & Katz (2015). These observed quantities are related to Eddington ratio, and so are an attempt to connect $R - L$ offsets with accretion rate while avoiding direct self-correlation with τ on both axes. The red lines show the best-fit relations to the Grier et al. (2017) SDSS-RM data, while the blue lines show the best-fit relations to all three samples. The $R - L$ offset is only marginally anti-correlated with the Hβ line widths in each case.

to the previous SEAMBH results (see Du et al. 2018, Figure 5) we estimate accretion rates for all three samples using two dimensionless quantities: Eddington ratio (calculated as described in Section 2) and $\dot{\mathcal{M}}$ (Equation 3, as defined in Du et al. 2016). The $R - L$ offsets of all three samples as a function of $\lambda_{\rm Edd}$ and $\dot{\mathcal{M}}$ are presented in Figure 9. Best-fit lines (with slope m and y-intercept b given in the figure legends) indicate significant ($> 5\sigma$) anti-correlations between $R - L$ offset and both estimators of accretion rate, with Spearman's $\rho \sim -0.50$ and $p \sim 10^{-11}$.

The anti-correlations in both panels of Figure 9 are qualitatively consistent with the simple self-correlations. To avoid these self-correlations, we instead study the dependence of $R - L$ offsets on accretion rate by using only the components of the Eddington ratio that are not computed directly from the the RM lag τ. Since $\lambda_{\rm Edd} \equiv \frac{L_{\rm bol}}{L_{\rm Edd}} \propto \frac{\lambda L_{5100}}{M_{\rm BH}}$ and $M_{\rm BH} \propto \tau v_{\rm fwhm}^2$, we examine the $R - L$ offset against two measurements of line width
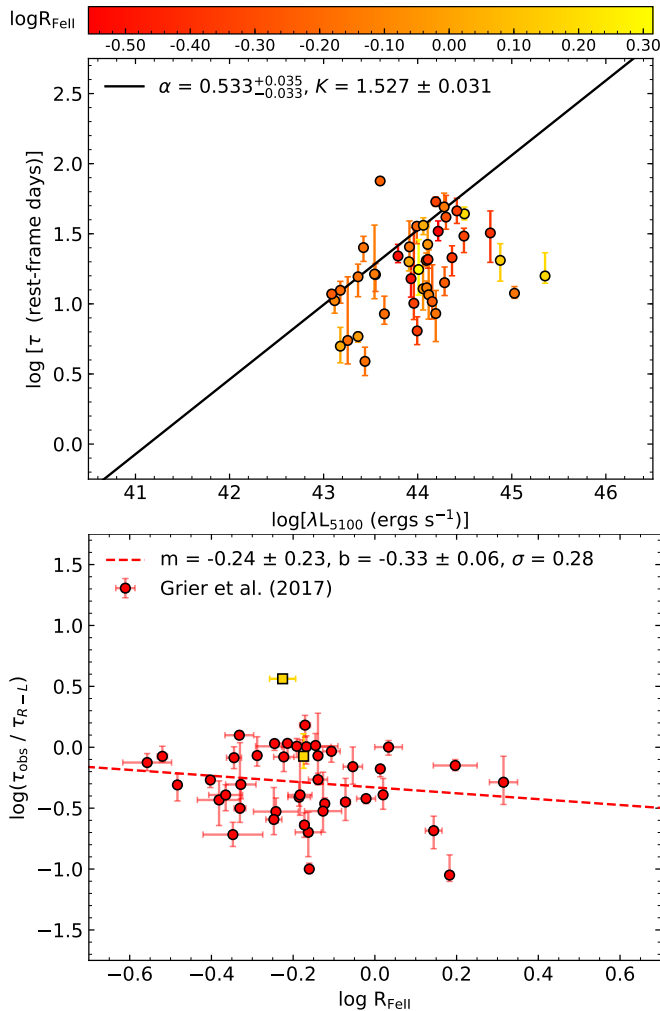
FIG. 11.— The $R - L$ relation for SDSS-RM quasars color-coded by the FeII effective strength R_{FeII} (top) and the $R - L$ offset τ_{obs}/τ_{R-L} versus R_{FeII} (bottom). Since R_{FeII} correlates with Eddington ratio (Shen & Ho 2014), a significant anti-correlation between $R-L$ offset and R_{FeII} would suggest that, at fixed luminosity, more rapidly accreting AGN have shorter lags. We do not observe a significant anti-correlation between $R - L$ offset and relative iron strength for SDSS-RM quasars, with a best-fit slope 1σ consistent with zero, and Spearman's $\rho = -0.11$ and $p = 0.49$.

v_{fwhm} and v_σ to determine if there are residual correlations beyond the self-correlations induced from λL_{5100} and τ appearing in both axes; this is presented in Figure 10. For all samples and for both line-width indicators, there are only marginal ($< 2\sigma$) anti-correlations between $R - L$ offset and Hβ broad-line width.

We make a final attempt at studying the relation between $R - L$ offset and accretion rate by using the relative FeII strength $R_{FeII} \equiv \frac{EW_{FeII}}{EW_{H\beta}}$. The relative FeII strength is one of the "Eigenvector 1" quantities that separate quasars into different spectral categories (Boroson & Green 1992), and in particular R_{FeII} correlates positively with Eddington ratio (Shen & Ho 2014). Thus we can use R_{FeII} as an independent estimate of accretion rate that avoids any self-correlation with τ_{obs}/τ_{R-L}. Figure 11 presents the relation between $R - L$ offset and R_{FeII} for the SDSS-RM AGN of Grier et al. (2017). We find no anti-correlation between offset and R_{FeII}, with a slope that is 1σ consistent with zero and Spearman's

$\rho = -0.11$ and $p = 0.49$. This is in contrast to the recent work of Du & Wang (2019), who found a significant correlation between $R-L$ offset and R_{FeII} using the SEAMBH and Bentz et al. (2013) AGN samples. We do find a consistent slope in the relation ($m = -0.24 \pm 0.23$ compared to $m = -0.42 \pm 0.06$ in Du & Wang 2019), and our anti-correlation may be marginal rather than significant due to the limited sample size of SDSS-RM, the different lag uncertainties of JAVELIN, and/or the greater diversity of AGN properties in the SDSS-RM sample.

4.2. $R - L$ Offset with UV Ionizing Luminosity

The $R - L$ relation is parameterized with the optical luminosity at rest-frame 5100 Å, but the response and size of the BLR is governed by the incident ionizing photons (e.g, Davidson 1972). In particular, the Hβ recombination line is driven by the incident luminosity of $E > 13.6$ eV photons. The basic photoionization expectation of $R \propto L^{0.5}$ is valid for the optical luminosity only if changes in optical luminosity also correspond to identical changes in the ionizing luminosity; however, the shape of the SED and therefore the ratio of UV and optical luminosities depends on factors like mass, accretion rate and spin (e.g., Richards et al. 2006). Modeling of the BLR by Czerny et al. (2019), with the assumption that the BLR radius is determined by the ionizing luminosity or number of incident photons, shows a diversity in the R-L relation due to changing UV/optical luminosity ratios, reproducing the range of observed lags from RM surveys. Additionally, emission-line lags relative to the optical continuum may be underestimated if there is an additional time lag between the UV-continuum and optical-continuum variability, as observed in NGC 5548 (Pei et al. 2017). However, lags between the UV and optical continua are short, so this would only significantly affect emission-line lags in the order of a few days.

None of our samples have published measurements of the $E > 13.6$ eV ionizing luminosity; however, the SDSS-RM sample has luminosity measurements at rest-frame 3000 Å and Hβ, better probing the (near-)UV compared to the optical λL_{5100}. Both of these quantities are shown with the $R-L$ offset of SDSS-RM AGN in Figure 12. We fit lines to each, finding that there is no anti-correlation between the $R - L$ offset and λL_{3000}, with Spearman's $\rho = -0.28$, $p = 0.09$. The best-fit line finds no significant (1σ) anti-correlation between the $R - L$ offset and the Hβ luminosity with Spearman's $\rho = -0.36$ and $p = 0.02$, additionally the $R - L$ relation color-coded by $L_{H\beta}$ (Figure 12 top right) indicates little variation of $L_{H\beta}/\lambda L_{5100}$ across the SDSS-RM sample.

The ratio of luminosities of the [OIII]$\lambda5007$ and Hβ emission lines is also frequently used as a proxy for the number of ionizing photons (e.g., Baldwin et al. 1981; Veilleux & Osterbrock 1987). Both are recombination lines, and [OIII] has an ionization energy of 55 eV compared to the H ionization energy of 13.6 eV. We find a significant (3.7σ) correlation between offset and $L_{[OIII]}/L_{H\beta}$, shown in Figure 13, with Spearman's $\rho = 0.36$, $p = 0.02$, and an excess scatter of ~ 0.24.

We conclude that the shape of the UV/optical SED is likely to play a role in the $R - L$ offset of AGN, as evident from the correlation with $L_{[OIII]}/L_{H\beta}$. The lack of significant correlations with λL_{3000} and $L_{H\beta}$ may be
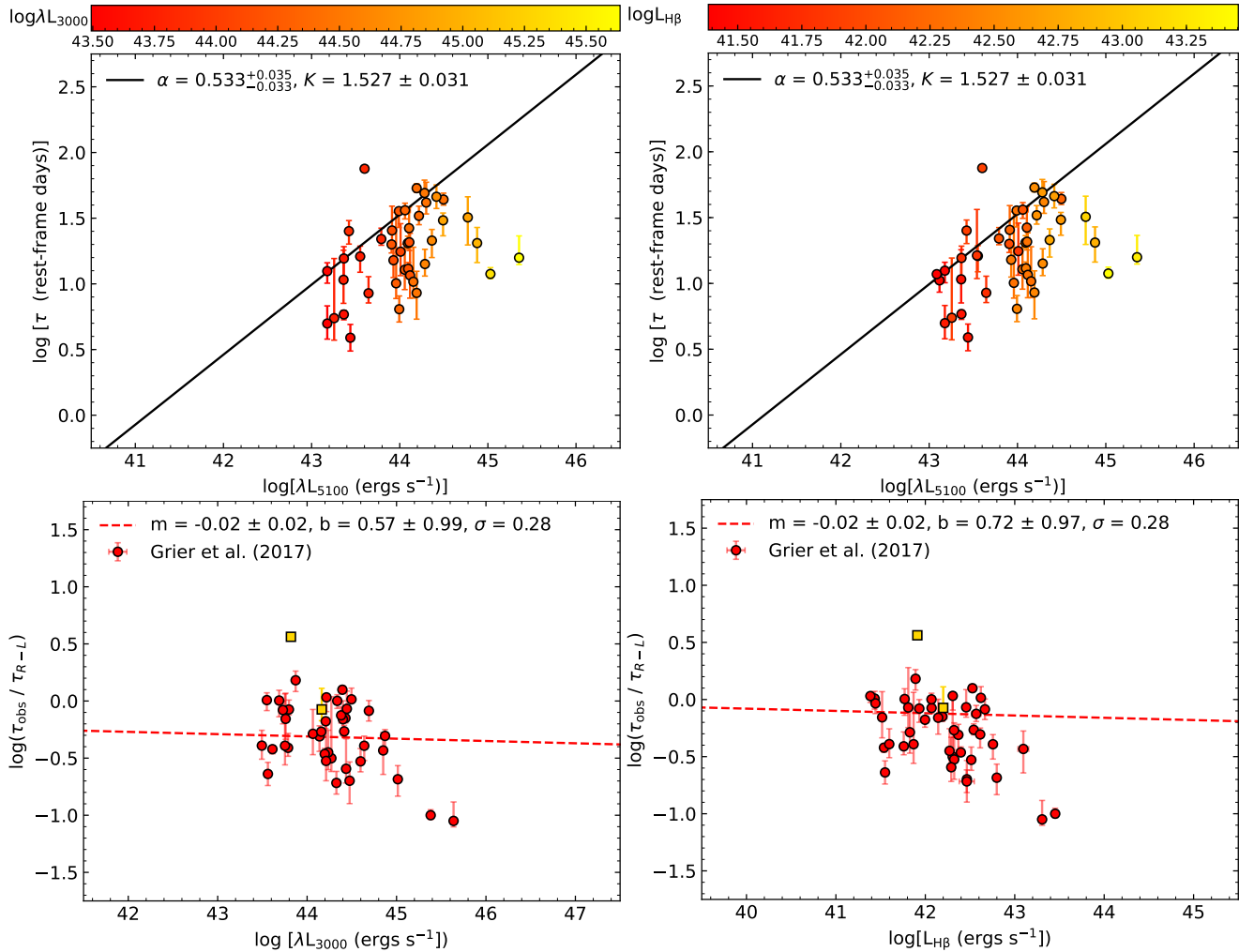
FIG. 12.— *Left:* The $R-L$ relation of SDSS-RM AGN color-coded by λL_{3000} and the $R-L$ offset $\tau_{\rm obs}/\tau_{R-L}$ versus λL_{3000}, a luminosity measurement closer to the ionizing UV luminosity than the λL_{5100} used in the $R-L$ relation. The sample spans a fairly narrow range of $\lambda L_{3000}/\lambda L_{5100}$ (top left) and the $R-L$ offset is not anti-correlated with λL_{3000} (slope 1σ from zero and Spearman's $\rho = -0.28$ and $p = 0.09$). *Right:* The $R-L$ relation of SDSS-RM AGN with the Hβ broad-line luminosity and the $R-L$ offset versus the Hβ broad-line luminosity, a proxy for the ionizing luminosity that drives Hβ recombination. Once more the sample spans a fairly narrow range of $L_{{\rm H}\beta}/\lambda L_{5100}$, and the $R-L$ offset and $L_{{\rm H}\beta}$ are not significantly correlated with a slope m that is 1σ consistent with zero, and Spearman's $\rho = -0.36$ and $p = 0.02$, with excess scatter of ~ 0.25 dex about the best-fit line.

because these luminosities do not accurately represent the luminosity of far-UV ($\lambda < 912$ Å) ionizing photons. The $L_{[{\rm OIII}]}/L_{{\rm H}\beta}$ ratio is likely tied to the broader shape of the AGN SED, which in turn is related to the accretion rate and/or black hole spin (e.g., Du et al. 2018; Czerny et al. 2019). It is a bit surprising that we find a significant correlation of $R-L$ offset with $L_{[{\rm OIII}]}/L_{{\rm H}\beta}$ but only a marginal anti-correlation with $R_{\rm FeII}$, given the observed anti-correlation between [O III] equivalent width and $R_{\rm FeII}$ (Figure 1 of Shen & Ho 2014). This may be due to the limited sample size of SDSS-RM AGN, and/or to the large uncertainties in its measured lags. Regardless of the root cause of the UV/optical SED changes, it would be valuable to add far-UV observations to the samples of SDSS-RM and SEAMBH AGN in order to directly compare their $R-L$ offsets with the luminosity of photons responsible for ionizing the BLR.

5. CONCLUSIONS

While previous RM studies revealed a tight "$R-L$" relation between the broad-line radius $R = c\tau$ and the

optical luminosity λL_{5100}, more recent studies (SDSS-RM and SEAMBH) frequently find shorter lags than expected for a given optical luminosity. We use Monte Carlo simulations that mimic the SDSS-RM survey design to show that the $R-L$ offsets are not solely due to observational bias. Instead, we find that AGN $R-L$ properties correlate most closely with AGN spectral properties: at fixed λL_{5100}, AGN have lower τ with lower $L_{[{\rm OIII}]}/L_{{\rm H}\beta}$. The correlation of $R-L$ offset with $L_{[{\rm OIII}]}/L_{{\rm H}\beta}$ is likely tied to changes in the UV/optical spectral shape. A more complete understanding of AGN $R-L$ properties will likely come from observations of the UV SED of RM AGN that directly measure the luminosity and shape of the ionizing continuum responsible for the AGN broad-line region.
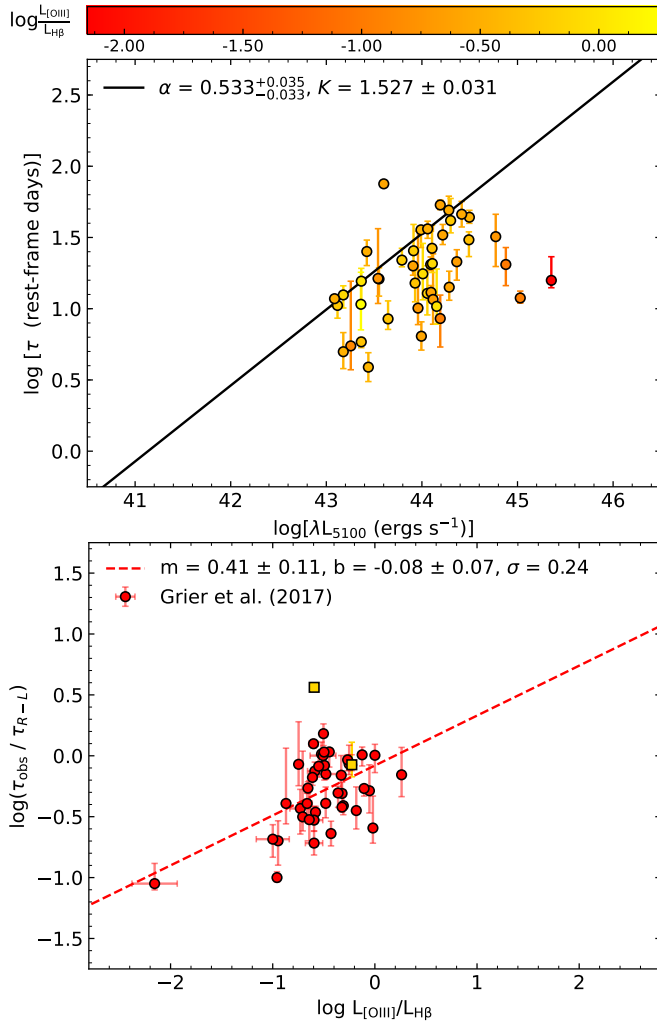
FIG. 13.— The $R - L$ relation of SDSS-RM color-coded by $L_{[\rm OIII]}/L_{\rm H\beta}$ (top) and the $R - L$ offset $\tau_{\rm obs}/\tau_{R-L}$ with $L_{[\rm OIII]}/L_{\rm H\beta}$ (bottom), an indicator of the far-UV ionizing flux present. AGN with larger (negative) $R - L$ offsets typically have lower $L_{[\rm OIII]}/L_{\rm H\beta}$, and there is a significant correlation between $\tau_{\rm obs}/\tau_{R-L}$ and $L_{[\rm OIII]}/L_{\rm H\beta}$ with a slope 3.7σ different from zero and a Spearman's $\rho = 0.36$ and $p = 0.02$.

REFERENCES

Baldwin, J. A., Phillips, M. M., & Terlevich, R. 1981, PASP, 93, 5
Bentz, M. C., & Katz, S. 2015, PASP, 127, 67
Bentz, M. C., Walsh, J. L., Barth, A. J., et al. 2009, ApJ, 705, 199
Bentz, M. C., Denney, K. D., Grier, C. J., et al. 2013, The Astrophysical Journal, 767, 149
Blandford, R. D., & McKee, C. F. 1982, ApJ, 255, 419
Boroson, T. A., & Green, R. F. 1992, ApJS, 80, 109
Collin, S., Kawaguchi, T., Peterson, B. M., & Vestergaard, M. 2006, A&A, 456, 75
Czerny, B., Wang, J.-M., Du, P., et al. 2019, ApJ, 870, 84
Davidson, K. 1972, ApJ, 171, 213
Dexter, J., Xin, S., Shen, Y., et al. 2019, arXiv e-prints, arXiv:1906.10138
Du, P., & Wang, J.-M. 2019, arXiv e-prints, arXiv:1909.06735
Du, P., Lu, K.-X., Zhang, Z.-X., et al. 2016, ApJ, 825, 126
Du, P., Zhang, Z.-X., Wang, K., et al. 2018, ApJ, 856, 6
Gaskell, C. M., & Peterson, B. M. 1987, ApJS, 65, 1
Grier, C. J., Martini, P., Watson, L. C., et al. 2013, ApJ, 773, 90
Grier, C. J., Trump, J. R., Shen, Y., et al. 2017, ApJ, 851, 21
Gunn, J. E., Siegmund, W. A., Mannery, E. J., et al. 2006, The Astronomical Journal, 131, 2332

Kaspi, S., Maoz, D., Netzer, H., et al. 2005, ApJ, 629, 61
Kaspi, S., Smith, P. S., Netzer, H., et al. 2000, ApJ, 533, 631
Kollmeier, J. A., Zasowski, G., Rix, H.-W., et al. 2017, arXiv e-prints, arXiv:1711.03234
Kormendy, J., & Ho, L. C. 2013, ARA&A, 51, 511
Li, I-Hsiu., Shen, Y., Brandt, W. N., et al. 2019, ApJ, 884, 119
Onken, C. A., Valluri, M., Peterson, B. M., et al. 2007, ApJ, 670, 105
Pancoast, A., Brewer, B. J., Treu, T., et al. 2014, MNRAS, 445, 3073
Pei, L., Fausnaugh, M. M., Barth, A. J., et al. 2017, ApJ, 837, 131
Peng, C. Y., Ho, L. C., Impey, C. D., & Rix, H.-W. 2002, AJ, 124, 266
Peterson, B. M., Ferrarese, L., Gilbert, K. M., et al. 2004, ApJ, 613, 682
Richards, G. T., Lacy, M., Storrie-Lombardi, L. J., et al. 2006, ApJS, 166, 470
Ross, N. P., McGreer, I. D., White, M., et al. 2013, ApJ, 773, 14
Shen, Y., & Ho, L. C. 2014, Nature, 513, 210
Shen, Y., Richards, G. T., Strauss, M. A., et al. 2011, The Astrophysical Journal Supplement Series, 194, 45

Shen, Y., Greene, J. E., Ho, L. C., et al. 2015a, ApJ, 805, 96

Shen, Y., Brandt, W. N., Dawson, K. S., et al. 2015b, ApJS, 216, 4

Shen, Y., Hall, P. B., Horne, K., et al. 2019, ApJS, 241, 34

Smee, S. A., Gunn, J. E., Uomoto, A., et al. 2013, The Astronomical Journal, 146, 32

Starkey, D. A., Horne, K., & Villforth, C. 2016, MNRAS, 456, 1960

Veilleux, S., & Osterbrock, D. E. 1987, ApJS, 63, 295

Wang, J.-M., Qiu, J., Du, P., & Ho, L. C. 2014a, ApJ, 797, 65

Wang, J.-M., Du, P., Hu, C., et al. 2014b, ApJ, 793, 108

White, R. J., & Peterson, B. M. 1994, PASP, 106, 879

Woo, J.-H., Yoon, Y., Park, S., Park, D., & Kim, S. C. 2015, ApJ, 801, 38

Yip, C. W., Connolly, A. J., Vanden Berk, D. E., et al. 2004, AJ, 128, 2603

Yu, L.-M., Bian, W.-H., Wang, C., Zhao, B.-X., & Ge, X. 2019, MNRAS, 488, 1519

Yu, Z., Kochanek, C. S., Peterson, B. M., et al. 2020, MNRAS, 491, 6045

Yue, M., Jiang, L., Shen, Y., et al. 2018, ApJ, 863, 21

Zu, Y., Kochanek, C. S., & Peterson, B. M. 2011, ApJ, 735, 80